Materials with the CrVO$_4$ structure type as candidate superprotonic conductors
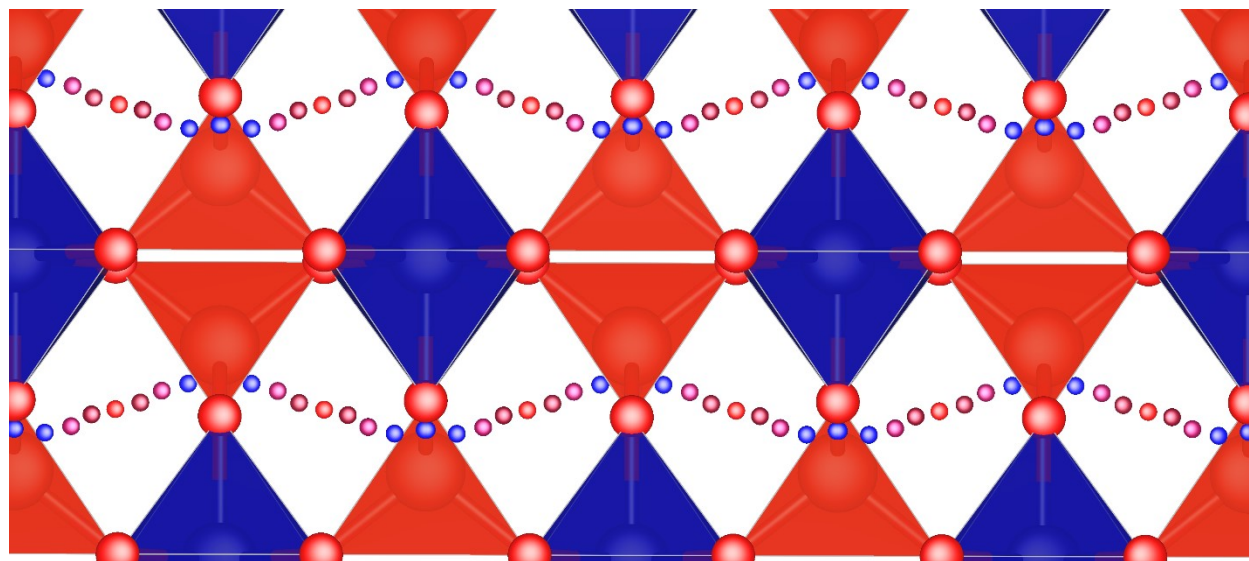
Pandu Wisesa,[a] Chenyang Li,[a] Chuhong Wang,[a] and Tim Mueller*[a]

Proton conducting oxides have the potential to improve the efficiency of solid oxide fuel cells and electrolyzers, yet many oxide structures remain relatively unexplored for the ability to conduct protons. To accelerate the search for novel proton-conducting oxides, we have performed a computational screen of the proton migration energy in 41 different commonly-occurring oxide structure types. The results of this screen, which are supported by a comprehensive set of density functional theory calculations, indicate that known materials with the CrVO$_4$ structure type have an average migration energy for proton diffusion of less than 0.2 eV, with several known materials having calculated migration energies below 0.1 eV. These results indicate that materials with the CrVO$_4$ structure type, which to our knowledge have not been previously explored as candidate proton conductors, may exhibit very high proton conductivity that surpasses that of leading proton-conducting oxides. We present the results of our screen as well as diffusion dimensionality analysis and thermodynamic stability analysis for materials with the CrVO$_4$ structure.

Department of Materials Science and Engineering, Johns Hopkins University, Baltimore, MD 21218, USA
E-mail: tmueller@jhu.edu
Electronic Supplementary Information (ESI) available

[a] Department of Materials Science and Engineering, Johns Hopkins University

1   Introduction

Proton-conducting solids are used in a variety of applications, including as hydrogen separation membranes in chemical processing[1-11] and in electrodes or electrolytes in solid oxide fuel cells[12-21] and electrolyzers.[22-26] There is particular interest in using proton-conducting oxides as electrolytes and electrode materials in fuel cells, where an electrolyte must be electronically insulating but an electrode material may be a mixed ionic-electronic conductor. A widely-used fuel cell technology, proton exchange membrane (PEM) fuel cells, uses polymer electrolytes that operate in an aqueous environment, so their operating temperatures are typically below 100 °C.[27, 28] At such low operating temperatures PEM cells require the use of expensive catalysts to achieve sufficiently high rates.[28] An alternative is to use a solid oxide that conducts oxygen ions for the electrolyte (and ideally the electrode as well), but to achieve sufficiently high rates such fuel cells typically need to be operated at temperatures above about 600 °C.[18, 29] There is increasing interest in developing fuel cells that can operate at intermediate temperature ranges, which could lower the cost of the fuel cells, reduce start-up times, improve efficiency, and improve long-term durability.[22, 29-32] As protons are smaller than oxygen ions and carry half the electronic charge, they tend to diffuse more readily than oxygen ions; thus a promising route to improving the rate capability (and lowering the operating temperature) of solid oxide fuel cells is to use proton-conducting oxides as electrolytes and electrode materials.[12-21] Fuel cells with proton-conducting electrolytes have additional advantages in that the reaction products are produced at the cathode, rather than the anode, so they are kept separate from the fuel, which can result in gains in efficiency.[13, 14] For fuel cells that use ammonia as a fuel, the use of proton-conducting electrolytes prevents the formation of NO, an unwanted byproduct.[17] Despite their advantages, fuel cells that use proton-conducting oxides are limited by a number of factors including poor proton transport through grain boundaries and poor stability in fuel cell operating conditions.[20, 33-36] To address these issues, there is a need to develop new proton-conducting oxides that are stable in fuel cell operating conditions and have high proton conductivity.

The most widely-studied class of proton-conducting oxides contains materials with the perovskite structure or closely related structures.[20, 34-42] A perovskite-structured material, $SrCeO_3$, was one of the first proton-conducting oxides with high proton conductivity,[43] and two of the current leading families of proton conducting oxides, based on $BaZrO_3$ and $BaCeO_3$, have the perovskite structure.[20, 34, 36] Perovskite-structured oxides can accommodate a wide variety of cations in different stoichiometries,[44] providing researchers great flexibility in tailoring their properties. Many perovskite-structured oxides can also accommodate high concentrations of oxygen vacancies and allow for relatively facile diffusion of oxygen ions, providing a mechanism to introduce protons into the host material through a reaction with water. Importantly, the arrangement of oxygen ions in the perovskite structure provides a continuous three-dimensional network for protons to migrate via the Grotthuss mechanism,[45] in which they rotate around oxygen ions and then hop between them. In the search for new proton-conducting oxides, researchers have increasingly been exploring materials that do not have the perovskite structure. These efforts have revealed proton conductivity in materials such as solid acids,[21, 46-48] ortho-niobates,[33] ortho-tantalates,[33, 49] orthophosphates,[50, 51] pyrochlores,[52] sesquioxides,[53] (oxy)sulfides,[54] nitrides,[55] tungstates,[56] tungsten oxide, where the Grotthuss mechanism was not observed,[57] and recently $Li_{13.9}Sr_{0.1}Zn(GeO_4)_4$ (LSZG).[58]

There are a number of criteria that must be met for a proton conductor to work in a fuel cell, electrolysis cell, or related technology. Among these, the material must be stable at operating

temperatures, resistant to poisoning, and selective. It must also have sufficiently high proton solubility. It is important to consider the electronic conductivity when assessing whether the material would be suitable for use as an electrolyte, membrane, or electrode material. However in all applications, it is necessary that the bulk mobility of protons through the material is high. There are on the order of 100,000 known inorganic materials,[59] but the bulk proton mobility is unknown for most materials, making it possible that there are entire classes of known materials that are good proton conductors but are currently being overlooked.

In this work we perform a high-throughput computational search to identify structure types that are likely to have high proton mobility. We focus on structure types rather than individual compounds as the ionic conductivity of a material is determined to a large extent by whether arrangement of cations and anions in the material is conducive to creating a potential energy surface with a low activation energy for ionic migration.[36, 60-62] Once a structure type conducive to proton mobility is identified, materials with that structure type and different chemical compositions can be designed and/or synthesized to try to find a material with high stability and proton solubility while maintaining a relatively high probability of having high proton mobility.

2   Methodology

We searched for promising structure types for proton conducting oxides using a multi-level screening approach. We first identified over 37,000 unique oxide materials with fully occupied sites from the Inorganic Crystal Structure Database (ICSD).[59] The structures were grouped by their structure types using an algorithm developed by our group to compare crystalline structures, resulting in 3,663 different oxide structure types. As we are most interested in structure types that can accommodate a variety of different elements, we selected from these the structure types for which the ICSD contained at least 20 unique materials, resulting in a data set of 41 structure types and 1946 structures in total.

We use the classical activation energy for proton migration (within the Born-Oppenheimer approximation) as our primary descriptor for proton mobility. We will refer to this value as the "migration energy". As the contribution to the material energy from the zero-point vibrational energy of protons can be large (~100-200 meV),[63, 64] there is likely a significant quantum contribution to proton mobility that is not captured by classical transition state theory. However even if quantum corrections are taken to account, it can be expected that materials with a lower classical activation energies will generally have faster proton migration.[65-67] Thus for the purposes of screening for promising proton conductors it is sufficient to use the classical migration energy.

The 1946 different oxide materials we consider contain 75 different elements. To calculate activation energies for proton migration in all 1946 materials it is necessary to use an energy model that works for most of the periodic table. As the use of first-principles methods such as density functional theory (DFT)[68, 69] for all materials in our data set would have been prohibitively expensive, we developed a simpler model based on the bond valence method,[70-74] which has been parameterized for nearly all elements.[75] In the bond valence model, the bond valence between two neighboring atoms is given by

$$s_{ij} = e^{\frac{R_0 - r}{b}} \qquad (1)$$

where s_{ij} is the bond valence, r is the bond length, and R_0 and b are parameters of the model. The valence of an atom is then given by the sum of the bond valences for bonds containing that atom. Here we have used the parameterization of Brese and O'Keefe,[75] in which b=0.37 and R_0 can be calculated for nearly any pair of elements in the periodic table.

The bond valence method relates the valence of a bond to the equilibrium bond length, but it cannot be used directly to calculate energies.[74, 76] However there is a natural relationship between the bond valence approach and electrostatic interactions[77] that makes it possible to construct a simple pairwise interatomic potential that is largely consistent with the bond valence model. Adams and Rao have developed a method for using the bond-valence method to construct a pairwise interatomic potential by combining a Morse-type term with a repulsive electrostatic term,[78] and they have used their approach to study lithium ion diffusion in battery materials.[79-81] Here we use a similar approach. The main difference between our approach and that of Adams and Rao is that the repulsive part of our potential is exponential, and attraction is represented by a screened Coulomb potential rather than a Morse potential. All electrostatic interactions, both attractive and repulsive, are thus combined in a single term:

$$E_{Coulomb} = k \frac{q_i q_j}{r} e^{\frac{-r}{d}}$$ (2)

where k is the Coulomb constant, q_i and q_j are the electrostatic charges of the two atoms, r is the distance between the two atoms, and d is the screening radius. Here we approximate the electrostatic charges to be proportional to the valence of the atoms as determine by the bond valence model, where the coefficient of proportionality and screening radius are determined by fitting to DFT data.

The repulsive part of the potential is given by:

$$E_{\exp} = A e^{-rC}$$ (3)

where r is the distance between two neighboring atoms, and A and C are constants for specific element pairs. The combined potential is then

$$E_{pair} = E_{Exp} + E_{Coulomb} \; .$$ (4)

To determine approximate values for A and C in equation (3), we use the fact that for a given set of atomic valences, the equilibrium bond length in equation (4) should match the bond length used to generate those valences in equation (1). For a given value of R_0, we find the values for A and C that minimize the mean squared difference between the equilibrium bond length and the value of r in equation (1) over seven different binary crystal structures: rhenium trioxide, cristabolite, cuprite, wurtzite (hexagonal), rutile, fluorite, rock salt, and cesium chloride. The values of A and C were then further refined by linearly scaling them using universal scale factors fit to DFT data. To

account for atomic relaxations from ideal crystalline sites in the presence of a proton, we connected each atom to its ideal site through a virtual spring, where the spring constant was a linear function of absolute value of the atomic charge. The parameters of this function were also fit to DFT data. Additional details about our approach, including the parameters used for our calculations, are provide in the Electronic Supplementary Information.

We used the above energy model to construct the potential energy surface for a single proton in the different oxide materials studied. We used a combination of a grid search, gradient descent, and structural symmetry to find saddle points, local minima, and diffusion pathways through each material. Starting from the proton site with the lowest potential energy, all possible diffusion pathways that fully crossed a unit cell were evaluated, and the pathway with the lowest maximum potential energy was selected as the most likely diffusion path. The migration energy for proton diffusion through the material was then calculated as the difference between the maximum and minimum potential energies along the most likely diffusion path.

2.1 Density functional theory calculations

All DFT calculations were done using the Vienna Ab-initio Simulation Package (VASP)[82-86] versions 5.3 and 5.4 using "accurate" precision. The electronic minimization was done using a combination of blocked Davidson iteration scheme and RMM-DIIS.[87, 88] Perdew-Burke-Ernzerhof (PBE)[89] projector augmented wave (PAW)[90] potentials were used for all calculations. To take into account of possible spin polarization in the material, all calculations are set to be spin polarized. The electronic self-consistency cutoff was set to 10^{-5} eV and the relaxation cutoff was set to 10^{-3} eV. The relaxation was done using the RMM-DIIS algorithm. The k-point grid was generated using the k-point grid server[91] with a minimum periodic distance of 28.1 Å. For thermodynamic stability calculations, we used the GGA+U approach of Dudarev.[92] We used a U-J value of 3.25 eV for vanadium, as determined by the Materials Project by fitting to the experimental formation energies of different vanadium oxides.[93] For cerium we used a value of 4.5 eV, which was determined self-consistently for Ce_2O_3 by Fabris et al.[94] and is close to the value of 5 eV determined empirically for $BaCeO_3$ by Shishkin and Ziegler.[95]

2.2 Nudged elastic band calculations

We used the climbing image nudged elastic band (CI-NEB) method as implemented in VASP by the Henkelman group.[96-100] The spring constant used for the elastic band was 5 eV/$Å^2$ and atomic relaxation was performed using damped molecular dynamics with scaling constant (POTIM) of 0.01. The energy model described above was run using experimental lattice parameters and atomic positions, as these are the values available from the ICSD. As the equilibrium structure in DFT calculations is typically slightly different from the experimentally-determined structure, we relaxed the volume of all structures using DFT prior to running NEB calculations. By relaxing the volume while leaving the fractional atomic coordinates unchanged, we ensured that it was straightforward to use the diffusion paths discovered using our energy model to initialize NEB calculations while avoiding spurious relaxations in DFT due to large stresses on the unit cell.

All NEB calculations were run in supercells of the relaxed unit cells that ensured there were at least 8 Å between periodic images. All NEB calculations were run at fixed volume and atomic positions were allowed to relax to create realistic models of proton diffusion in the dilute limit.[35, 101] For each diffusive hop, the NEB images were initialized by placing hydrogen atoms along the

path of the hop with no more than 0.5625 Å between successive hydrogen locations. The end points of the NEB calculation had their lattice vector frozen and atomic positions relaxed.

Oxides are typically doped with an electron acceptor to incorporate protons into the lattice. As this would break symmetry and significantly increase the computational expense of our calculations, we generated training data for our energy model using a perfect (undoped) crystal in which a single electron was removed per diffusing hydrogen atom in the NEB calculations. To minimize discontinuities due to spin flips during the NEB calculations, the magnetic moments on all atoms in each image were fixed to the values of the relaxed, empty (without hydrogen) structure. The conjugate gradient algorithm was used for atomic relaxation in all NEB runs. The relaxation was stopped when forces converged within 0.05 eV/Å. All other parameters were the same as those listed in the above section on density functional theory calculations.

2.3   Stability of doped phases

We used PyMatGen[102] to identify the likely decomposition products of the doped compositions from the Materials Project database, and we calculate the energies of the doped phases and possible decomposition products using DFT as described above. For the DFT calculations we assume the dopants are distributed in a way that maximizes the distance between dopant atoms in the resulting materials, and we use our energy model to calculate the likely position of H in the doped material.

3   Results

3.1   Migration energies of the training data

The parameterized potential model was able to predict the migration barriers energies of the 52 structures in our training set (Table 3-S in the ESI) with a mean absolute error of 0.126 eV (Figure 1) relative to DFT. Within the set of 52 training structures, there are four structure types that are represented by at least five structures: cubic perovskite, hexagonal perovskite, elpasolite, and spinel. Much of the noise in the fit disappears when we evaluate the average activation energies for each of these structure types (Figure 1B), and the mean absolute error between the potential model and DFT decreases to 0.032 meV. This reduction in error can be understood by considering a simple model in which the migration energy can be expressed as the sum of two components: the average migration energy for materials with that structure type, and the deviation from this average due to the chemical composition of the material. The total prediction error (Figure 1A) will be a sum of the errors for each of these components. If the parameter fitting produces a model for which the mean error in the chemical composition component is nearly zero, then even if the variance of this error is large its contribution to the overall error can be greatly reduced by averaging over different chemical compositions.
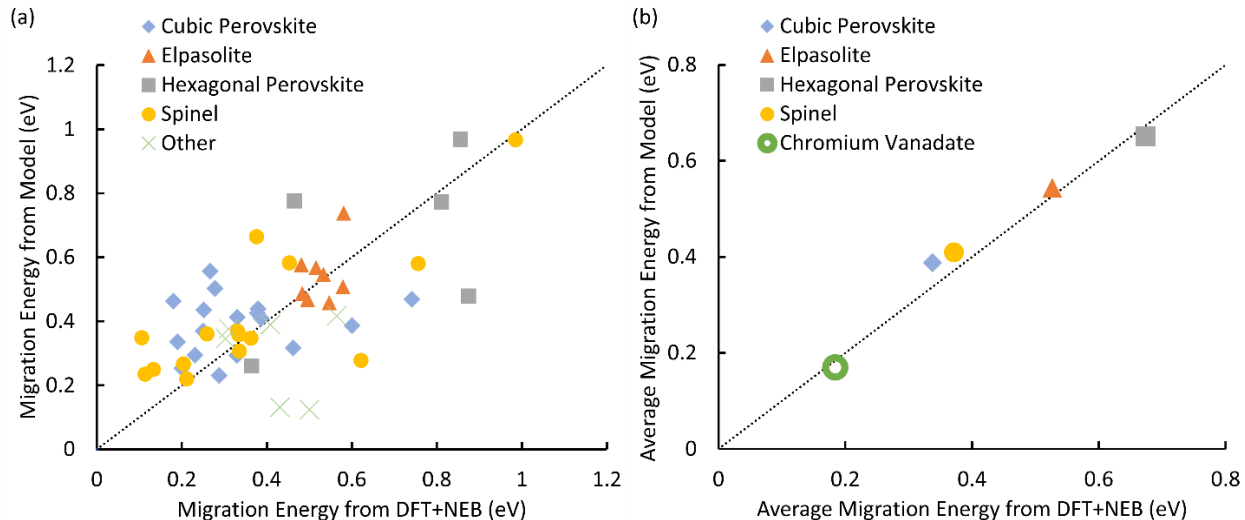
Figure 1. (a) A plot of activation energy for proton migration calculated by DFT+NEB vs. predicted by the energy model. Structure types with less than 5 members in the dataset are put together and represented by the green cross. (b) A plot of average migration energy by structure type calculated by DFT+NEB vs. predicted by the energy model. The filled shapes correspond to the training data in part (a), and the empty green circle represents the $CrVO_4$ structure type discovered by our screen, with the DFT activation energy averaged over all 29 structures in Table 2. In both (a) and (b) the diagonal dotted line represents perfect agreement.

As expected, our calculations show that the average migration energy for cubic perovskites, the most studied class of proton conductors, is relatively low. Our DFT-calculated activation energies are consistent with those reported by Bork et al.[103] A typical diffusion pathway in a cubic perovskite, $BaZrO_3$, is shown in Figure 2. The pathway predicted by the energy model, including the locations of the end points and saddle points, corresponds well to DFT+NEB pathways. Diffusion occurs via a Grotthuss-type mechanism, where the proton rotates around the oxygen atom before hopping to the next oxygen atom. Protons also diffuse through hexagonal perovskites via a Grotthuss-type mechanism (Figure 2), but the hexagonal perovskites in our training data have nearly twice the average activation energies of cubic perovskites even though they share the same composition of ABX_3, providing an indication of the importance of structure type in determining activation energies.
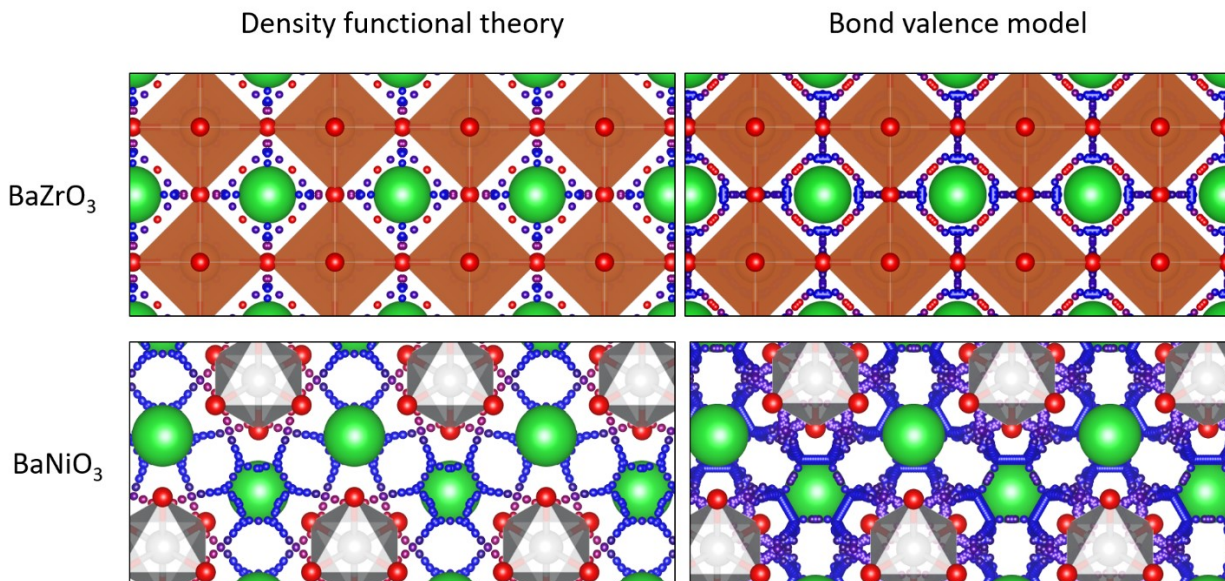
Figure 2. Ab-initio (left) and model-predicted (right) diffusion pathways in a cubic perovskite (top) and hexagonal perovskite (bottom). Large green spheres represent barium atoms, orange polyhedra contain zirconium, and grey polyhedra contain nickel. Small spheres represent the possible diffusion pathways with warm (more red) colors representing high energy sites and cool (more blue) colors representing low energy sites.

3.3   Screening structure types

We used our model to predict the activation energies for proton diffusion in all 1946 test structures, representing 41 different structure types with at least 20 oxide materials per type. On average, predicting the average migration energy for a structure type took around 20 minutes on a single core, which is a small fraction of the cost of DFT+NEB calculations. The average activation energies per by structure type are provide in Table 1 and Figure 3. We note that the average activation energies for cubic perovskite, hexagonal perovskite, spinel, and elpasolite are different than the averages shown in Figure 1, as these averages were taken over all oxide structures in the ICSD rather than just those in our training set.

The structure types with the highest predicted average activation energies are elpasolite, hexagonal perovskite, $CuFeO_2$, Delafossite-$NaCrS_2$, and Sr_2NiWO_6. The average activation energies for proton diffusion in these structure types is about 200 meV higher than the average for cubic spinel, which at 600 °C would correspond to a more than 10-fold decrease in proton mobility assuming an Arrhenius-type dependence on migration energy. However within these structure types there can be significant variation in activation energies among individual materials (Table 1), leaving open the possibility that some materials with these structure types may be competitive as proton conductors.

There are 11 oxide structure types for which the predicted average activation energies are below that of cubic perovskite, and nearly 20 more with average activation energies within 100 meV. This suggests that materials with a variety of different structure types could have proton mobilities competitive with cubic perovskites. The fifth-best structure type, a monoclinic fergusonite, has

been experimentally investigated for proton conductivity. Several rare-earth niobates and tantalates with this structure type have demonstrated proton conductivity on the order of 10^{-4} - 10^{-3} S/cm at about 700 °C, making them among the best known proton conductors outside the Ba- and Sr-based cubic perovskites.[33] Many materials of this class transform to a high-temperature scheelite phase (#10 on our list) that has similar proton conductivity.[33, 104] The ninth-best structure type, pyrochlore, has also been investigated for proton conductivity.[52, 105] Materials of this type have demonstrated proton conductivity on the order of 10^{-4} - 10^{-3} S/cm at about 800 °C.[105]

Table 1. A ranking of 41 oxide structure types screened by the model based on their average migration energy.

Rank	Average Migration Energy (eV)	Sample Standard Deviation (eV)	Structure Type Name	Number of Materials	Space Group
1	0.193	0.105	$CrVO_4$	29	$Cmcm$
2	0.312	0.099	Calcite	20	$R\bar{3}c$
3	0.326	0.084	Zircon	64	$I4_1/amd$
4	0.332	0.067	$NaMn_7O_{12}$	30	$Im\bar{3}$
5	0.333	0.074	Fergusonite	27	$C2/c$
6	0.359	0.154	Spinel - Al_2MgO_4	64	$Fd\bar{3}m$
7	0.364	0.105	Rutile	41	$P4_2/mnm$
8	0.382	0.089	$LiYb(WO_4)_2$	30	$P2/n$
9	0.391	0.100	Pyrochlore	91	$Fd\bar{3}m$
10	0.402	0.129	Scheelite	43	$I4_1/a$
11	0.421	0.093	$ZrCuSiAs$ - $CuHfSi_2$	57	$P4/nmm$
12	0.432	0.241	Cubic Perovskite	88	$Pm\bar{3}m$
13	0.439	0.107	Barite-$BaSO_4$	23	$Pnma$
14	0.445	0.129	$Sc_2Si_2O_7$	23	$C2/m$
15	0.458	0.121	Th_2TeN_2	24	$I4/mmm$
16	0.460	0.094	Olivine	44	$Pnma$
17	0.461	0.101	Tilted Perovskite	161	$Pnma$
18	0.477	0.231	PbClF	29	$P4/nmm$
19	0.479	0.067	Quaternary Double Perovskite	47	$P2_1/n$
20	0.484	0.118	Pyroxene-$CaMg(SiO_3)_2$	35	$C2/c$
21	0.491	0.093	Monazite	20	$P2_1/n$
22	0.492	0.085	$CaFe_2O_4$	30	$Pnma$
23	0.492	0.091	$BaCuY_2O_5$	26	$Pnma$
24	0.493	0.068	Double Perovskite	96	$P2_1/n$
25	0.501	0.271	Fluorite-CaF_2	15	$Fm\bar{3}m$
26	0.505	0.064	Bi_2ErO_4I	38	$P4/mmm$
27	0.513	0.052	Sr_2NiWO_6	34	$I4/m$
28	0.516	0.181	Rocksalt	28	$Fm\bar{3}m$

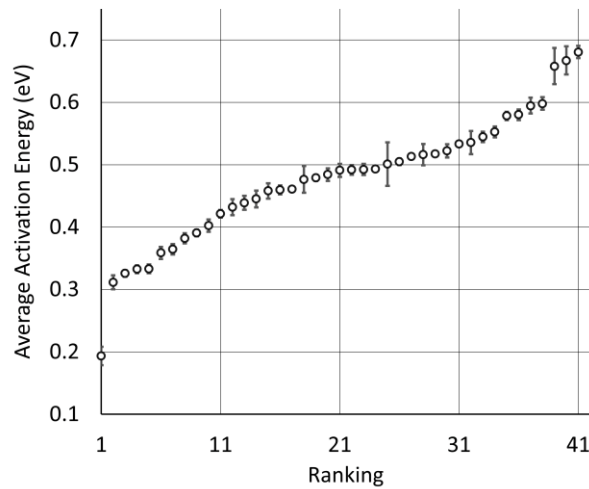| 29	0.517	0.079	Elpasolite	121	$Fm\bar{3}m$
30	0.522	0.133	La_2O_3	40	$P\bar{3}m1$
31	0.533	0.035	Apatite	17	$P6_3/m$
32	0.536	0.231	K_2MgF_4	39	$I4/mmm$
33	0.545	0.075	$La_3NbO_7(OS)$	21	$Cmcm$
34	0.553	0.131	K_4CdCl_6	56	$R\bar{3}c$
35	0.578	0.081	Melilite	39	$P\bar{4}2_1m$
36	0.580	0.108	K_2SO_4	41	$Pnma$
37	0.595	0.170	Delafossite	45	$R\bar{3}m$
38	0.598	0.088	Bixbyite-Mn_2O_3	19	$Ia\bar{3}$
39	0.658	0.296	Delafossite-$NaCrS_2$	26	$R\bar{3}m$
40	0.667	0.169	$CuFeO_2$	14	$P6_3/mmc$
41	0.681	0.124	Hexagonal Perovskite	40	$P6_3/mmc$

Figure 3. Plot of the ranking shown in Table 1, along with calculated standard errors of the averages. $CrVO_4$ is represented by the dot near 0.2 on the left.

The four structure types with the lowest average activation energies are $CrVO_4$, calcite, zircon, and $NaMn_7O_{12}$. $NaMn_7O_{12}$ is a cubic double-perovskite structure closely related to the cubic perovskites.[106] To our knowledge, the remaining three structure types have never been studied for proton conductivity. Of these, the $CrVO_4$ structure type is an outlier in our analysis (Figure 3), with a predicted average migration energy more than 0.1 eV below that of the next-best structure type, suggesting exceptionally high proton mobility. We have investigated the prediction of our model by using DFT to calculate the activation energies for proton migration in all 29 materials with this structure type in the ICSD (Table 2). We have used both DFT and DFT+U to calculate proton migration barriers (Section 4 in the ESI) and found that the mean absolute difference is only 34 meV and the mean difference is only 2 meV, suggesting low sensitivity of these results to the U values. The average DFT-calculated migration energy, 184 meV, is in excellent agreement with the

model prediction (Figure 1). These low activation energies for diffusion suggest that some materials with the $CrVO_4$ structure type may be superprotonic conductors.

Table 2. Calculated properties for the 29 known $CrVO_4$-structured oxides in the ICSD.

ICSD ID	Composition	Energy Above Hull (eV/atom)	Predicted Activation Migration Energy for 1D Diffusion (eV)	Predicted Activation Migration Energy for 2D Diffusion (eV)	Predicted Activation Migration Energy for 3D Diffusion (eV)	DFT Calculated Migration Energy (eV)
16618	$InPO_4$	0.000	0.084	0.427	0.870	0.340
16619	$TlPO_4$	0.000	0.159	0.473	0.841	0.270
16741	$NiSO_4$	0.000	0.067	0.389	0.865	0.161
16759	$MgSO_4$	0.000	0.048	0.433	0.959	0.234
18117	$MgCrO_4$	0.000	0.259	0.430	0.775	0.094
18118	$CdCrO_4$	0.000	0.212	0.518	0.620	0.056
23492	$CoCrO_4$	0.000	0.232	0.414	0.873	0.094
23493	$NiCrO_4$	0.000	0.228	0.306	0.875	0.053
25700	$NiSeO_4$	0.000	0.219	0.421	0.906	0.249
31231	$MnSO_4$	0.000	0.386	0.386	0.669	0.217
60571	$CdSO_4$	0.000	0.135	0.470	0.924	0.177
82286	VPO_4	0.000	0.070	0.367	0.810	0.196
155162	$InVO_4$	0.000	0.246	0.494	0.881	0.054
416147	$HgCrO_4$	0.000	0.270	0.551	0.943	0.085
23507	$FeSO_4$	0.001	0.075	0.437	0.725	0.159
33736	$CoSO_4$	0.002	0.048	0.437	0.752	0.229
109070	$MgSeO_4$	0.002	0.140	0.447	0.935	0.282
109071	$MnSeO_4$	0.002	0.133	0.465	0.923	0.165
109072	$CoSeO_4$	0.005	0.158	0.444	0.918	0.256
36244	$CrVO_4$	0.007	0.275	0.338	0.881	0.172
109073	$CuSeO_4$	0.007	0.128	0.462	0.898	0.295
82161	$FeVO_4$	0.015	0.214	0.459	0.897	0.262
62159	$CrPO_4$	0.018	0.048	0.366	0.848	0.242
155065	$FePO_4$	0.021	0.037	0.428	0.862	0.195
183216	$CuCrO_4$	0.031	0.152	0.383	0.853	0.154
82282	$TiPO_4$	0.074	0.167	0.311	0.627	0.321
159272[a]	$AlPO_4$	0.106	0.091	0.218	0.846	0.161
89505	$LiMnO_4$	0.143	0.242	0.444	0.831	0.086
166436[b]	$TiSiO_4$	0.156	0.054	0.437	0.695	0.091

[a] The $CrVO_4$ structure type has been identified as that of the high-pressure phase.[107]

[b] The $CrVO_4$ structure type was computationally determined to be the lowest-energy polymorph,[108] but to our knowledge it has never been synthesized.

$CrVO_4$, has an orthorhombic lattice, with one-dimensional columns of CrO_6 octahedra linked together by sharing common oxygen atoms with VO_4 tetrahedra. It is generally the stable structure

for compositions in which the crystal radius of the octahedrally-coordinated ion is between 0.75 and 1.1 Å, and the crystal radius of the tetrahedrally-coordinated ion is between 0.25 and 0.5 Å.[109] Proton diffusion is predicted to preferentially occur along a one-dimensional path through the lattice perpendicular to the columns of CrO_6 octahedra (Figure 4). As with most oxides, proton conduction is predicted to occur via a Grotthuss-type mechanism where the proton rotates around on oxygen ion and then jumps to another. Large rotations of the tetrahedra, as observed in $CsH_2(PO_4)$,[110] are not required for proton migration. Because the potential energy surface along the diffusion path fairly flat, the local minimum varies from material to material, and the jump between the oxygen ions sometimes represents the local minimum along the diffusion path (Figure 4). As our energy model sometimes identifies the wrong local minimum along this path due the small energy differences between the local minima and the transition states (Figure 4), we manually evaluated different possible local minima for many of the DFT nudged-elastic-band calculations.
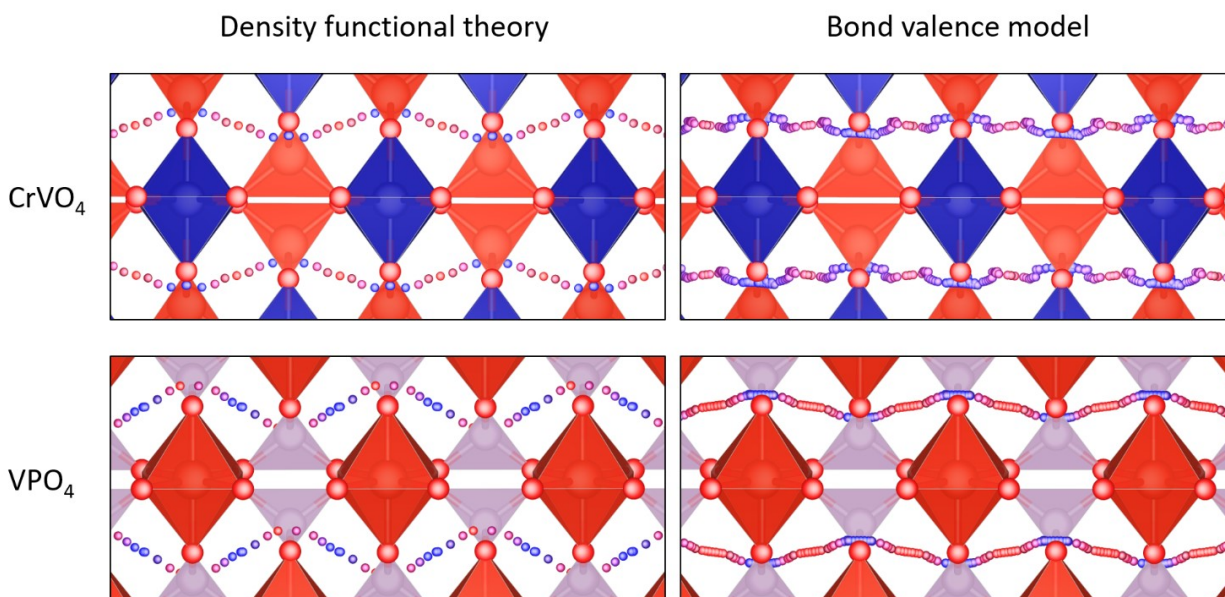

Figure 4. Fastest diffusion paths for VPO_4 and $CrVO_4$, which are the representatives of the $CrVO_4$ structure type. Red tetrahedra represent the bonds between vanadium and oxygen blue tetrahedra represent the bonds between chromium and oxygen, and purple tetrahedra represent PO_4^{-3}. Small blue and red spheres represent the diffusion pathway, with blue indicating low energy sites and red indicating high energy sites.

Ionic conductivity in one dimension presents practical challenges, as defects that block the diffusion channel could significantly inhibit diffusivity.[111] For this reason it is important to assess the ability of protons to migrate around defects by diffusing in a second dimension. We have used our model to calculate the minimum migrations energies required for one-, two-, and three-dimensional diffusion in each of the 29 materials with the $CrVO_4$ structure type (Table 2). As we ran some of these calculations with denser grids to ensure convergence in all three dimensions, the average migration energy in one dimension is slightly below that reported in Table 1. The directions

through the crystal along which one-, two-, and three-dimensional diffusion are predicted to occur most readily are shown in Figure 5. The average migration energy required for diffusion in two dimensions is 419 meV, which is approximately the calculated average migration energy for diffusion in cubic perovskites. This suggests that in many of these materials there will likely be an acceptably fast path around any defects that block the fastest diffusion channels. Diffusion in three dimensions has an average predicted migration energy of 838 meV, indicating that diffusion at competitive rates will likely be limited to two dimensions in these materials. In practice, the degree to which the single dimensionality of the highly conductive channel limits lithium ion conductivity will vary by material based on both the two-dimensional migration energy in that material and the defect density.
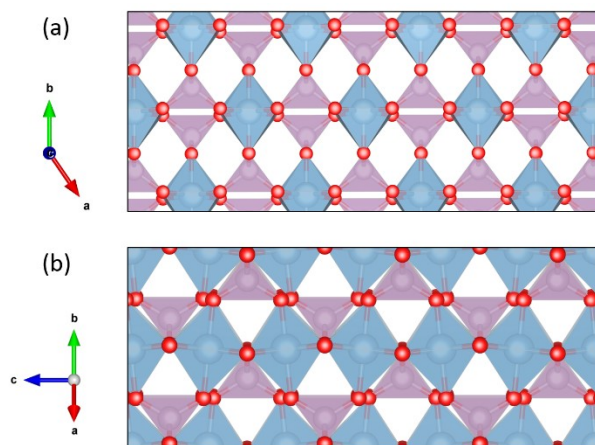

Figure 5. The structure of $CrVO_4$ family represented by $AlPO_4$. Blue spheres in the tetrahedra represent aluminum, and purple tetrahedra represents PO_4^{-3} ions. The fastest diffusion path is left-to-right in a), and the second-fasted diffusion path is left-to-right (along the c axis) in b).

Proton conduction depends on both proton mobility and proton concentration in the material. As none of the known $CrVO_4$-structured materials intrinsically contain hydrogen atoms, it would be necessary to introduce protons into these materials. In some materials this might be accomplished through redox reactions with transition metals or by hydrating intrinsic oxygen vacancies. However in many cases it will likely be necessary to introduce protons by doping the materials with electron acceptors, as is commonly done in proton-conducting oxides.[12] The conductivity of the doped materials will depend on the concentration of protons (and dopants) that can be introduced without sacrificing stability.

To assess the stability of the doped and undoped materials, we use a DFT-calculated convex hull of stable phases, which provides the energy of the thermodynamically stable phase or combination of phases as a function of composition.[112-114] The 0K DFT-calculated energy relative to the convex hull has been shown to be a useful descriptor for stability and synthesizability.[115] This value is an estimate of the thermodynamic driving force for decomposition, with a value of 0 indicating a stable material. Most known oxides have energies within about 15 meV/atom of the convex hull, and 90% of known oxides have energies within about 62 meV/atom of the convex hull.[115] The energies above the convex hull for the 29 known $CrVO_4$-structured materials, calculated using data from the

Materials Project, are provided in Table 2. Fourteen of the twenty-nine materials are on the DFT-calculated convex hull, and another eleven are within 35 meV/atom of the hull. Of the remaining four, one ($AlPO_4$) is a high-pressure phase, and another ($TiSiO_4$) has never been synthesized to our knowledge. The $CrVO_4$ structure type is predicted to be the lowest-energy polymorph of $TiSiO_4$,[108] but as it is calculated to be 156 meV / atom above the convex hull we believe $TiSiO_4$ is unlikely to exist in a form stable enough for practical use.

We assess the thermodynamic stability of the doped phases in a similar way. The widely-studied proton conducting oxides $BaZrO_3$ and $BaCeO_3$ are typically doped with about 10% (mole fraction) Y,[12] resulting in nominal compositions of $H_{0.1}Y_{0.1}BaZr_{0.9}O_3$ and $H_{0.1}Y_{0.1}BaCe_{0.9}O_3$. We predict these materials to be 19 meV/atom and 36 meV/atom above the convex hull, respectively. For comparison, we have performed similar calculations on two promising $CrVO_4$-structured materials, VPO_4 and $InVO_4$, doped with 10% Mg. The doped materials, with nominal compositions of $H_{0.1}Mg_{0.1}V_{0.9}PO_4$ and $H_{0.1}Mg_{0.1}In_{0.9}VO_4$, have DFT-calculated energies that are 5 meV/atom and 18 meV/atom above the hull, respectively. These results indicate that doping is likely to be a viable strategy for incorporating practically high concentrations of protons into materials with the $CrVO_4$ structure type.

Materials with the $CrVO_4$ structure type are generally composed of common, non-precious elements (Table 2). Our calculations indicate that most of them are electronically insulating, with a band gap of greater than 1 eV as calculated using GGA/GGA+U (Section 4 in the ESI). They have been studied for their magnetic properties[116, 117] and as possible battery electrodes.[118-120] However although all of the known $CrVO_4$-structured materials are predicted to have low migration barriers for protons, with DFT-calculated values ranging from 53 to 340 meV, to our knowledge no materials in this class have been investigated as possible proton conductors. Of particular note is $InVO_4$, a compound with high chemical stability and a melting point of 1134 °C,[109] that has been extensively studied as a photocatalyst for H_2 production.[121-123] It has recently been shown that thin, single crystals of $InVO_4$ also serve as efficient catalysts for CO_2 photoreduction in the presence of water vapor.[121] The DFT-calculated proton migration barrier in $InVO_4$ is only 54 meV, and its ability to rapidly transport protons may play a role in its catalytic properties for reactions involving protons.

Conclusions

A high-throughput computational screen has identified materials with the $CrVO_4$ structure type as likely to have very low migration energies for the one-dimensional diffusion of protons, and this prediction is supported by density functional theory calculations on known $CrVO_4$-structured materials. In practice proton conduction may be limited by the one-dimensional nature of the path for rapid migration; the average migration energy for two-dimensional diffusion is predicted to be comparable to that of leading structure types for proton conduction. A thermodynamic assessment of acceptor-doped $CrVO_4$-structured materials indicates that this structure type is capable of hosting competitively high concentrations of protons without creating an unacceptably large thermodynamic driving force for decomposition. Known materials with this structure type are typically composed of common, non-precious elements, providing flexibility to chemically tailor their properties materials and investigate different strategies for proton incorporation. These results indicate that $CrVO_4$-structured materials are a promising new area for exploration in the search for new proton-conducting oxides.

Conflicts of interest

There are no conflicts to declare.

Acknowledgements

References

1. R. Bredesen, K. Jordal and O. Bolland, *Chemical Engineering and Processing: Process Intensification*, 2004, **43**, 1129-1158.
2. R. W. Baker, *Ind. Eng. Chem. Res.*, 2002, **41**, 1393-1411.
3. J. W. Phair and S. P. S. Badwal, *Sci. Technol. Adv. Mater.*, 2006, **7**, 792-805.
4. J. W. Phair and S. P. S. Badwal, *Ionics*, 2006, **12**, 103-115.
5. P. o. S. T. f. I. Reuse, Recycling, C. o. I. T. Assessments, C. o. Engineering, T. Systems and N. R. Council, *Separation Technologies for the Industries of the Future*, The National Academies Press, 1998.
6. M. T. a. R. Inc., Case Study: Hydrogen Separations in Syngas Processes, http://www.mtrinc.com/case_study/h2_co_ratio_adjustment_in_syngas_production.html, 2014).
7. S. Tosti, A. Basile, G. Chiappetta, C. Rizzello and V. Violante, *Chemical Engineering Journal*, 2003, **93**, 23-30.
8. G. Barbieri, A. Brunetti, A. Caravella and E. Drioli, *RSC Advances*, 2011, **1**, 651-661.
9. S. Uemiya, N. Sato, H. Ando and E. Kikuchi, *Ind. Eng. Chem. Res.*, 1991, **30**, 585-589.
10. H. Malerød-Fjeld, D. Clark, I. Yuste-Tirados, R. Zanón, D. Catalán-Martinez, D. Beeaff, S. H. Morejudo, P. K. Vestre, T. Norby, R. Haugsrud, J. M. Serra and C. Kjølseth, *Nature Energy*, 2017, **2**, 923-931.
11. S. H. Morejudo, R. Zanón, S. Escolástico, I. Yuste-Tirados, H. Malerød-Fjeld, P. K. Vestre, W. G. Coors, A. Martínez, T. Norby, J. M. Serra and C. Kjølseth, *Science*, 2016, **353**, 563-566.
12. E. Fabbri, D. Pergolesi and E. Traversa, *Chem. Soc. Rev.*, 2010, **39**, 4355-4369.
13. A. Demin and P. Tsiakaras, *International Journal of Hydrogen Energy*, 2001, **26**, 1103-1108.
14. W. G. Coors, *Journal of Power Sources*, 2003, **118**, 150-156.
15. W. Jamsak, S. Assabumrungrat, P. L. Douglas, N. Laosiripojana, R. Suwanwarangkul, S. Charojrochkul and E. Croiset, *Chemical Engineering Journal*, 2007, **133**, 187-194.
16. M. Ni, D. Y. C. Leung and M. K. H. Leung, *Journal of Power Sources*, 2008, **183**, 133-142.
17. Q. Ma, R. Peng, Y. Lin, J. Gao and G. Meng, *Journal of Power Sources*, 2006, **161**, 95-98.
18. C. Duan, J. Tong, M. Shang, S. Nikodemski, M. Sanders, S. Ricote, A. Almansoori and R. O'Hayre, *Science*, 2015, **349**, 1321-1326.
19. J. R. G. Taillades, J. Dailly, N. Fukatsu, and R. H. A. Magrasó, and P. R. Slater, in *Proton-Conducting Electrolytes for Solid Oxide Fuel Cell Applications*, ed. M. Marrony, 2016, DOI: 10.1007/978-3-319-46146-5_3, ch. Chapter 2, pp. 73-146.
20. N. Kochetova, I. Animitsa, D. Medvedev, A. Demin and P. Tsiakaras, *Rsc Advances*, 2016, **6**, 73222-73268.
21. S. M. Haile, D. A. Boysen, C. R. I. Chisholm and R. B. Merle, *Nature*, 2001, **410**, 910-913.
22. L. Bi, S. Boulfrad and E. Traversa, *Chem. Soc. Rev.*, 2014, **43**, 8255-8270.
23. M. A. Laguna-Bercero, *Journal of Power Sources*, 2012, **203**, 4-16.
24. S. Giddey, S. P. S. Badwal and A. Kulkarni, *International Journal of Hydrogen Energy*, 2013, **38**, 14576-14594.
25. I. Garagounis, V. Kyriakou, A. Skodra, E. Vasileiou and M. Stoukides, *Frontiers in Energy Research*, 2014, **2**.

26. E. Vøllestad, R. Strandbakke, M. Tarach, D. Catalán-Martínez, M.-L. Fontaine, D. Beeaff, D. R. Clark, J. M. Serra and T. Norby, *Nature Materials*, 2019, **18**, 752-759.
27. D. Carter and J. Wing, *The Fuel Cell Industry Review 2013*, 2013.
28. A. Hauch, S. D. Ebbesen, S. H. Jensen and M. Mogensen, *Journal of Materials Chemistry*, 2008, **18**, 2331-2340.
29. Z. Gao, L. V. Mogni, E. C. Miller, J. G. Railsback and S. A. Barnett, *Energy & Environmental Science*, 2016, **9**, 1602-1644.
30. D. J. L. Brett, A. Atkinson, N. P. Brandon and S. J. Skinner, *Chem. Soc. Rev.*, 2008, **37**.
31. E. D. Wachsman and K. T. Lee, *Science*, 2011, **334**, 935-939.
32. J. A. Kilner and M. Burriel, *Annual Review of Materials Research*, 2014, **44**, 365-393.
33. R. Haugsrud and T. Norby, *Nature Materials*, 2006, **5**, 193-196.
34. M. Marrony and P. Pan Stanford, *Proton-conducting ceramics from fundamentals to applied research*, Pan Stanford Publishing, Singapore, 2016.
35. W. Munch, K. D. Kreuer, G. Seifert and J. Maier, *Solid State Ionics*, 2000, **136**, 183-189.
36. K. D. Kreuer, *Annual Review of Materials Research*, 2003, **33**, 333-359.
37. Q. Zhang, G. Wahnstrom, M. E. Bjorketun, S. Gao and E. Wang, *Phys Rev Lett*, 2008, **101**, 215902.
38. M. A. Gomez and F. J. Liu, *Solid State Ionics*, 2013, **252**, 40-47.
39. J. A. Dawson and I. Tanaka, *Journal of Materials Chemistry A*, 2015, **3**, 10045-10051.
40. K. D. Kreuer, *Solid State Ionics*, 1997, **97**, 1-15.
41. F. Shimojo, *Solid State Ionics*, 1998, **113-115**, 319-323.
42. E. Matsushita and T. Sasaki, *Solid State Ionics*, 1999, **125**, 31-37.
43. H. Iwahara, T. Esaka, H. Uchida and N. Maeda, *Solid State Ionics*, 1981, **3-4**, 359-363.
44. M. A. Peña and J. L. G. Fierro, *Chem. Rev.*, 2001, **101**, 1981-2018.
45. C. J. T. de Grotthuss, *Mémoire sur la décomposition de l'eau: et des corps qu' elle tient en dissolution à l'aide de l'électricité galvanique*, publisher not identified, 1805.
46. C. R. I. Chisholm, Y. H. Jang, S. M. Haile and W. A. Goddard, *Physical Review B*, 2005, **72**.
47. B. C. Wood and N. Marzari, *Physical Review B*, 2007, **76**.
48. O. Barron, H. N. Su, V. Linkov, B. G. Pollet and S. Pasupathi, *Journal of Applied Electrochemistry*, 2014, **44**, 1037-1045.
49. R. Haugsrud and T. Norby, *Journal of the American Ceramic Society*, 2007, **90**, 1116-1121.
50. K. Amezawa, Y. Tomii and N. Yamamoto, *Solid State Ionics*, 2003, **162**, 175-180.
51. N. Hatada, K. Toyoura, T. Onishi, Y. Adachi and T. Uda, *Journal of Physical Chemistry C*, 2014, **118**, 29629-29635.
52. K. Toyoura, A. Nakamura and K. Matsunaga, *Journal of Physical Chemistry C*, 2015, **119**, 8480-8487.
53. T. Norby, O. Dyrlie and P. Kofstad, *J. Am. Ceram. Soc.*, 1992, **75**, 1176-1181.
54. J. M. Polfus, T. Norby and R. Bredesen, *J. Phys. Chem. C*, 2015, **119**, 23875-23882.
55. J. M. Polfus and R. Haugsrud, *Solid State Commun.*, 2012, **152**, 1921-1923.
56. R. Haugsrud, *Solid State Ionics*, 2007, **178**, 555-560.
57. H. Lin, F. Zhou, C. P. Liu and V. Ozolins, *Journal of Materials Chemistry A*, 2014, **2**, 12280-12288.
58. T. Wei, L. A. Zhang, Y. Chen, P. Yang and M. L. Liu, *Chemistry of Materials*, 2017, **29**, 1490-1495.
59. *Journal*.
60. Y. Wang, W. D. Richards, S. P. Ong, L. J. Miara, J. C. Kim, Y. Mo and G. Ceder, *Nat Mater*, 2015, **14**, 1026-1031.
61. K.-D. Kreuer, *Chemistry of Materials*, 1996, **8**, 610-641.
62. A. Van der Ven, J. Bhattacharya and A. A. Belak, *Acc Chem Res*, 2013, **46**, 1216-1225.
63. C. Wolverton, V. Ozoliņš and M. Asta, *Physical Review B*, 2004, **69**, 144109.
64. D. E. Jiang and E. A. Carter, *Physical Review B*, 2004, **70**, 064102.

65. G. Henkelman, A. Arnaldsson and H. Jonsson, *The Journal of Chemical Physics*, 2006, **124**, 044706-044709.
66. B. C. Garrett and D. G. Truhlar, *The Journal of Physical Chemistry*, 1979, **83**, 200-203.
67. E. Wigner, *Transactions of the Faraday Society*, 1938, **34**, 29-41.
68. P. Hohenberg and W. Kohn, *Physical Review B*, 1964, **136**, B864-+.
69. W. Kohn and L. J. Sham, *Physical Review*, 1965, **140**, 1133-&.
70. L. Pauling, *Journal of the American Chemical Society*, 1929, **51**, 1010-1026.
71. I. D. Brown and R. D. Shannon, *Acta Crystallographica Section A*, 1973, **29**, 266-282.
72. D. Altermatt and I. D. Brown, *Acta Crystallographica Section B-Structural Science*, 1985, **41**, 240-244.
73. W. L. Bragg, *Journal*, 1930, **74**, 237.
74. I. D. Brown, *Chem Rev*, 2009, **109**, 6858-6919.
75. M. O'Keefe and N. E. Brese, *Journal of the American Chemical Society*, 1991, **113**, 3226-3229.
76. S. Adams and J. Swenson, *Physical Review B*, 2000, **63**.
77. C. Preiser, J. Losel, I. D. Brown, M. Kunz and A. Skowron, *Acta Crystallographica Section B*, 1999, **55**, 698-711.
78. S. Adams and R. P. Rao, *Phys. Chem. Chem. Phys.*, 2009, **11**, 3210-3216.
79. S. Adams and R. P. Rao, *Journal of Materials Chemistry*, 2012, **22**, 1426-1434.
80. S. Adams and R. P. Rao, *Solid State Ionics*, 2011, **184**, 57-61.
81. S. Adams and R. P. Rao, *physica status solidi (a)*, 2011, **208**, 1746-1753.
82. G. Kresse and J. Hafner, *Phys Rev B Condens Matter*, 1993, **47**, 558-561.
83. G. Kresse and J. Hafner, *Phys Rev B Condens Matter*, 1994, **49**, 14251-14269.
84. G. Kresse and J. Furthmuller, *Physical Review B*, 1996, **54**, 11169-11186.
85. G. Kresse and J. Furthmuller, *Computational Materials Science*, 1996, **6**, 15-50.
86. G. Kresse and D. Joubert, *Physical Review B*, 1999, **59**, 1758-1775.
87. D. M. Wood and A. Zunger, *Journal of Physics a-Mathematical and General*, 1985, **18**, 1343-1359.
88. P. Pulay, *Chemical Physics Letters*, 1980, **73**, 393-398.
89. J. P. Perdew, K. Burke and M. Ernzerhof, *Phys Rev Lett*, 1996, **77**, 3865-3868.
90. P. E. Blochl, *Physical Review B*, 1994, **50**, 17953-17979.
91. P. Wisesa, K. A. McGill and T. Mueller, *Physical Review B*, 2016, **93**, 155109.
92. S. L. Dudarev, G. A. Botton, S. Y. Savrasov, C. J. Humphreys and A. P. Sutton, *Physical Review B*, 1998, **57**, 1505-1509.
93. A. Jain, S. P. Ong, G. Hautier, W. Chen, W. D. Richards, S. Dacek, S. Cholia, D. Gunter, D. Skinner, G. Ceder and K. A. Persson, *APL Materials*, 2013, **1**, 011002.
94. S. Fabris, G. Vicario, G. Balducci, S. de Gironcoli and S. Baroni, *The Journal of Physical Chemistry B*, 2005, **109**, 22860-22867.
95. M. Shishkin and T. Ziegler, *Surface Science*, 2012, **606**, 1078-1087.
96. G. Henkelman, B. P. Uberuaga and H. Jonsson, *Journal of Chemical Physics*, 2000, **113**, 9901-9904.
97. G. Henkelman and H. Jonsson, *Journal of Chemical Physics*, 2000, **113**, 9978-9985.
98. D. Sheppard, R. Terrell and G. Henkelman, *J Chem Phys*, 2008, **128**, 134106.
99. D. Sheppard and G. Henkelman, *J Comput Chem*, 2011, **32**, 1769-1771; author reply 1772-1763.
100. D. Sheppard, P. Xiao, W. Chemelewski, D. D. Johnson and G. Henkelman, *J Chem Phys*, 2012, **136**, 074103.
101. P. G. Sundell, M. E. Björketun and G. Wahnström, *Physical Review B*, 2007, **76**, 094301.
102. S. P. Ong, W. D. Richards, A. Jain, G. Hautier, M. Kocher, S. Cholia, D. Gunter, V. L. Chevrier, K. A. Persson and G. Ceder, *Computational Materials Science*, 2013, **68**, 314-319.
103. N. Bork, N. Bonanos, J. Rossmeisl and T. Vegge, *Physical Review B*, 2010, **82**, 014103.
104. R. Haugsrud and T. Norby, *Solid State Ionics*, 2006, **177**, 1129-1135.

105. T. Omata and S. Otsuka-Yao-Matsuo, *Journal of The Electrochemical Society*, 2001, **148**, E252-E261.
106. M. Marezio, P. D. Dernier, J. Chenavas and J. C. Joubert, *Journal of Solid State Chemistry*, 1973, **6**, 16-20.
107. J. Pellicer-Porres, A. M. Saitta, A. Polian, J. P. Itié and M. Hanfland, *Nature Materials*, 2007, **6**, 698.
108. L. Gracia, A. Beltrán and D. Errandonea, *Physical Review B*, 2009, **80**, 094105.
109. E. J. Baran, *Journal of Materials Science*, 1998, **33**, 2479-2497.
110. G. Kim, J. M. Griffin, F. Blanc, S. M. Haile and C. P. Grey, *J. Am. Chem. Soc.*, 2015, **137**, 3867-3876.
111. R. Malik, D. Burch, M. Bazant and G. Ceder, *Nano Letters*, 2010, **10**, 4123-4127.
112. A. A. Emery and C. Wolverton, *Scientific Data*, 2017, **4**, 170153.
113. S. Curtarolo, D. Morgan and G. Ceder, *Calphad*, 2005, **29**, 163-211.
114. D. Hildebrandt and D. Glasser, *The Chemical Engineering Journal and the Biochemical Engineering Journal*, 1994, **54**, 187-197.
115. W. Sun, S. T. Dacek, S. P. Ong, G. Hautier, A. Jain, W. D. Richards, A. C. Gamst, K. A. Persson and G. Ceder, *Science Advances*, 2016, **2**, e1600225.
116. B. C. Frazer and P. J. Brown, *Physical Review*, 1962, **125**, 1283-1291.
117. M. J. Isasi, R. Saezpuche, M. L. Veiga, C. Pico and A. Jerez, *Materials Research Bulletin*, 1988, **23**, 595-601.
118. M. E. Arroyo-de Dompablo, J. M. Gallardo-Amores, M. T. Azcondo, F. García-Alvarado and U. Amador, *Journal of Physics and Chemistry of Solids*, 2006, **67**, 1243-1247.
119. X. Liang, X. Ou, H. Dai, F. Zheng, Q. Pan, P. Liu, X. Xiong, M. Liu and C. Yang, *Chemical Communications*, 2017, **53**, 12696-12699.
120. S. Denis, E. Baudrin, M. Touboul and J. M. Tarascon, *Journal of The Electrochemical Society*, 1997, **144**, 4099-4109.
121. Q. Han, X. Bai, Z. Man, H. He, L. Li, J. Hu, A. Alsaedi, T. Hayat, Z. Yu, W. Zhang, J. Wang, Y. Zhou and Z. Zou, *J. Am. Chem. Soc.*, 2019, **141**, 4209-4213.
122. J. Ye, Z. Zou, M. Oshikiri, A. Matsushita, M. Shimoda, M. Imai and T. Shishido, *Chemical Physics Letters*, 2002, **356**, 221-226.
123. R. V. d. Krol, J. Ségalini and C. S. Enache, *Journal of Photonics for Energy*, 2011, **1**, 1-11, 11.
124. K. Momma and F. Izumi, *Journal of Applied Crystallography*, 2011, **44**, 1272-1276.

<div align="center">

Electronic Supplementary Information for

"Materials with the CrVO₄ structure type as candidate superprotonic conductors"

Pandu Wisesa, Chenyang Li, Chuhong Wang, and Tim Mueller[*]

</div>

1. Finding oxidation states and charges

The bond valence-based energy model requires that every atom in the material is assigned a nominal oxidation state. To determine the oxidation states for the elements, we use the following algorithm:

1. For a given structure, list all the likely oxidation states for all the elements in the structure. We used the information from the book Chemistry of the Elements, 2nd Edition by Greenwood and Earnshaw[1] to create this list. We assign a prior likelihood to each oxidation state based on the count of the oxidation state in ICSD[2]. We also checked the rarity for a given oxidation state and incremented (or decremented) the count based on whether the oxidation state is never known before (decrement of 5), rare (increment of 10), or common (increment of 50). The relative counts of each state for a given element allow us to determine the prior probability, $P(oxidation)$, of the element achieving that state.

2. For each atom in the structure, calculate the valence, BV, predicted by the bond-valence method.

3. Let $P(BV \mid oxidation)$ be calculated using a Gaussian distribution over the difference between the atomic valence any given oxidation state. The standard deviation of this distribution was set to be 1. We can the calculate the probability of any oxidation state for a given valence using Bayes' theorem:

$$P(oxidation \,|\, BV) = P(BV \,|\, oxidation)P(oxidation) \tag{1}$$

4. Consider all possible combinations of oxidation states in the structure that preserve charge balance and select the one that maximizes the product of $P(oxidation \,|\, BV)$ over all atoms.

The oxidation states are not necessarily equal to the physical charge at each site, but for simplicity we approximated the effective charge to be proportional to the oxidation state. Thus the effective charge of each site was calculated by multiplying the oxidation state by a constant factor, q_s:

$$q = q_s \times (\text{oxidation state}) \tag{2}$$

The charge scaling factor q_s was one of the parameters fit to DFT calculations.

2. Treatment of solids and relaxation

To take into account the possible relaxation of atoms in the solids, we treat the atoms in the solid as if they are attached to their ideal lattice sites with springs, where the spring constant k is defined as:

$$k = k_0 + k_s |q| \tag{1}$$

where k_0 is the base value of the spring constant, k_s is a charge-scaling factor, and q is the charge for a given site.

In the presence of a diffuser, an atom is assumed to relax from its ideal site by a distance of r_{offset}. The pair interaction, accounting for relaxations, is then:

$$E_{relax}(r) = E_{pair}(r + r_{offset}) + \frac{k}{2}(r_{offset})^2 \tag{2}$$

where r is the ideal distance between the atoms.

To find the value of r_{offset} at equilibrium, the force between the two atoms must be zero:

$$0 = \frac{dE_{relax}(r)}{dr_{offset}} = E_{pair}'(r + r_{offset}) + kr_{offset} \ . \tag{3}$$

We approximate $E_{pair}'(r + r_{offset})$ using Taylor expansion:

$$E_{pair}'(r + r_{offset}) \approx E_{pair}'(r) + E_{pair}''(r) r_{offset} \tag{4}$$

substituting equation (2.4) to equation (2.3):

$$0 = \frac{dE_{relax}(r)}{dr_{offset}} \approx E_{pair}'(r) + E_{pair}''(r) r_{offset} + kr_{offset} \tag{5}$$

$$r_{offset} \approx \frac{-E_{pair}{}'(r)}{E_{pair}{}''(r) + k} \quad . \tag{6}$$

The above expression allows us to rapidly estimate the value of r_{offset} and approximately account

for atomic relaxation in our energy model.

3. Energy model construction and parameters

To screen for potential proton conductors, we employed a simple energy model that combines an exponential repulsion term backed with a Coulomb screening term:

$$E_{pair} = E_{Exp} + E_{Coulomb} \qquad (7)$$

where

$$E_{Coulomb} = k \frac{q_i q_j}{r} e^{\frac{-r}{d}} \qquad (8)$$

$$E_{exp} = Ae^{-rC}. \qquad (9)$$

The exponential repulsion term is backed by the bond-valence parameters and model found by Brese and O'Keefe[3]:

$$R_o = r_i + r_j - \frac{r_i r_j (\sqrt{c_i} - \sqrt{c_j})^2}{c_i r_i + c_j r_j} \qquad (10)$$

where r_i, r_j, c_i, and c_j are element specific parameters provided by Brese and O'Keefe.

Initial values for the parameters A and C (we will call these A_0 and C_0) were found using the following algorithm:

1. Determine the effective charges for the atoms in the material using the approach described in section 1.

2. For each atom in the structure, calculate the R_o value between that atom and hydrogen from O'Keefe and Brese's parameters and equation. This is the initial R_o and we will call it R_{o_init}.

3. Scale R_{o_init} with a universal scaling factor, r_s , such that $R_{o\_s} = R_{o\_init} r_s$. We scaled the value of R_o because O'Keefe and Brese showed that while the R_o values found from their model show a linear correlation with the real observed bond distances, the value they had for hydrogen is an outlier.[3]

4. For each of the following structure types,

    a. Rhenium trioxide

    b. Cristabolite

    c. Cuprite

    d. Wurtzite (hexagonal)

    e. Rutile

    f. Fluorite

    g. Rock salt

    h. Cesium chloride,

    find the bond valence s_{ij} between anions and cations based on the coordination number.

5. Using the value of s_{ij} and R_{o_s} found above, calculate the ideal r for every given structure using the bond valence relationship, $s_{ij} = \exp\left(\dfrac{R_o - r}{b}\right)$.

6. Fit A_0 and C_0 by minimizing the difference between the equilibrium bond lengths for the energy model and ideal r values found in step 6. The values for A_0 and C_0 found this way are shown in Table 1-S

Table 1-S. The values of A_0 *and* C_0 for different elements from the algorithm above before scaling factor is applied.

Atomic Number	Element Name	A_0 value (eV)	C_0 value (1/Å)
1	hydrogen	221.9308	6.326371
3	lithium	1488.779	5.987387
4	beryllium	855.2014	6.058016
5	boron	807.1233	6.054705
6	carbon	818.045	6.050931
7	nitrogen	724.9243	6.068031
8	oxygen	575.4666	6.104692
9	fluorine	393.2073	6.164485
11	sodium	12387.92	6.433914
12	magnesium	2926.124	5.907983
13	aluminum	2417.579	5.949664
14	silicon	2304.041	5.935647
15	phosphorus	2172.857	5.932193
16	sulfur	1928.756	5.965598
17	chlorine	1743.925	5.967689
19	potassium	39767.03	6.245923
20	calcium	19687.23	6.363112
21	scandium	10919.34	6.400903
22	titanium	3418.643	5.86216
23	vanadium	3030.132	5.91109
24	chromium	2627.325	5.927545
25	manganese	2682.867	5.913579
26	iron	2615.633	5.917104
27	cobalt	2097.285	5.935246
28	nickel	1802.869	5.951649
29	copper	1065.052	6.02664
30	zinc	1978.228	5.948852
31	gallium	2504.425	5.918385
32	germanium	3047.044	5.909144
33	arsenic	3211.198	5.876663
34	selenium	3107.699	5.899439
35	bromine	2721	5.930455
37	rubidium	20451	5.732408
38	strontium	11571.63	5.771011
39	yttrium	7618.364	5.813256
40	zirconium	13426.42	6.304055
41	niobium	5372.929	5.853688
42	molybdenum	4870.293	5.8563
44	ruthenium	2976.293	5.903065

45	rhodium	2804.601	5.92546
46	palladium	2171.285	5.941574
47	silver	2247.833	5.934706
48	cadmium	3977.844	5.928631
49	indium	12185.16	6.441506
50	tin	5193.418	5.857844
51	antimony	9265.984	6.10237
52	tellurium	17296.56	6.384611
53	iodine	4866.394	5.851438
55	cesium	105654.4	6.104346
56	barium	23628.27	5.731376
57	lanthanum	37704.82	6.250221
58	cerium	12127.21	5.756003
59	praseodymium	11849.48	5.780223
60	neodymium	10987.64	5.778148
62	samarium	10245.66	5.798301
63	europium	10392.85	5.789439
64	gadolinium	9151.173	5.794684
65	terbium	9149.794	5.832182
66	dysprosium	8339.335	5.822479
67	holmium	9062.617	5.883528
68	erbium	7322.257	5.811325
69	thulium	7133.626	5.816795
70	ytterbium	6862.874	5.818053
71	lutetium	17959.58	6.379059
72	hafnium	15323.36	6.399602
73	tantalum	5506.245	5.883319
74	tungsten	5085.098	5.851917
75	rhenium	4922.541	5.849618
77	iridium	4992.275	5.850301
80	mercury	4271.098	5.874973
81	thallium	11094.77	5.795774
82	Lead	8600.042	5.826843
83	bismuth	8769.27	5.808584
90	thorium	14500.64	5.80836
92	uranium	9543.9	5.79126

For cation-cation interactions, the value of A was calculated by multiplying A_0 by a universal scaling constant a_s:

$$A = A_0 a_s \tag{11}$$

For anion-cation interactions, we did not scale the value of A. A similar approach was used for C. For an anion-cation interaction:

$$C_{eff} = \frac{C}{a_c} \tag{12}$$

and for a cation-cation interaction

$$C_{eff} = c_c C \tag{13}$$

Altogether, there are eight parameters (such as the scaling factors) for the energy model that were determined by fitting to DFT-calculated activation energies of a training set of 52 materials. The list of eight parameters and their final values are shown in Table 2-S, and the training data are summarized in Table 3-S.

Table 2-S. Parameters used in the model and their values after fitting. q_e is the elementary charge.

Symbol	Parameter	Value	Unit
k_0	Spring constant base value	5	eV / Å^2
k_s	Spring constant scaling	4	eV / (q$_e$ Å^2)
d	Screening radius for Coulomb interaction	0.71	Angstrom
q_s	Charge scaling	0.42	
a_s	Cation-cation scaling term for A	0.83	
a_c	Anion-cation scaling term for C	0.79	
c_c	Cation-cation scaling term for C	0.90	
r_s	Universal R_o-value scale	0.91	

Fitting to DFT calculations was done incrementally using a grid search using the Pearson correlation coefficient as the primary metric after accounting for outliers identified using the average error and standard deviation of the predicted values. We started with the cubic perovskite

crystal class, then added hexagonal perovskite, spinel, elpasolite and other randomly selected structure. Through this method we were able to rapidly identify a good region of parameter space and then refine our values. The outcome of the final fitting process for the 52 training structures is shown in Table 3-S:

Table 3-S. The 52 structures used to train the model.

Composition	Oxide Structure Type	Model Predicted Activation Energy (eV)	DFT+NEB Calculated Activation Energy (eV)	Absolute Difference (eV)
Ca_2MgWO_6	Alternating Perovskite	0.416737	0.564008	0.147271
$CrSrO_3$	Cubic Perovskite	0.25348	0.19972	0.053759
$CaTiO_3$	Cubic Perovskite	0.317002	0.46147	0.144468
$MoSrO_3$	Cubic Perovskite	0.386586	0.599814	0.213228
$KTaO_3$	Cubic Perovskite	0.409248	0.386502	0.022745
$GePbO_3$	Cubic Perovskite	0.293683	0.3292	0.035517
$CaSiO_3$	Cubic Perovskite	0.426016	0.37739	0.048626
$NaWO_3$	Cubic Perovskite	0.294477	0.230381	0.064096
$KCrO_3$	Cubic Perovskite	0.375982	0.309166	0.066816
$SrZrO_3$	Cubic Perovskite	0.469067	0.741086	0.272019
$BaTiO_3$	Cubic Perovskite	0.369738	0.249483	0.120255
$BaZrO_3$	Cubic Perovskite	0.502707	0.27732	0.225387
$BaIrO_3$	Cubic Perovskite	0.439164	0.378972	0.060192
$BaSnO_3$	Cubic Perovskite	0.463129	0.179522	0.283607
$BaPbO_3$	Cubic Perovskite	0.556238	0.266042	0.290196
$SrNbO_3$	Cubic Perovskite	0.412975	0.330074	0.082901
$BaNbO_3$	Cubic Perovskite	0.435342	0.251341	0.184001
$LaAlO_3$	Cubic Perovskite	0.230819	0.287421	0.056601
$SrTiO_3$	Cubic Perovskite	0.335922	0.189221	0.1467
Ba_2NiO_6Re	Elpasolite	0.737628	0.580371	0.157257
GaO_6SbSr_2	Elpasolite	0.567261	0.514962	0.052299
Ba_2MgWO_6	Elpasolite	0.546621	0.532571	0.01405
Ba_2FeMoO_6	Elpasolite	0.507778	0.578513	0.070736
Ba_2FeReO_6	Elpasolite	0.458289	0.546507	0.088218
Ba_2ZnReO_6	Elpasolite	0.486157	0.48288	0.003277
Ba_2CoReO_6	Elpasolite	0.577129	0.480684	0.096445
Ba_2MoNiO_6	Elpasolite	0.467585	0.495648	0.028063
$BaSiO_3$	Hexagonal Perovskite	0.479127	0.87437	0.395243
$BaNiO_3$	Hexagonal Perovskite	0.773659	0.810901	0.037242
$BaRuO_3$	Hexagonal Perovskite	0.776816	0.464395	0.312421

BaCoO$_3$	Hexagonal Perovskite	0.968349	0.855273	0.113075
LaCrO$_3$	Hexagonal Perovskite	0.26082	0.363617	0.102797
Si$_2$Sc$_2$O$_7$	Pyrocholre	0.388962	0.40772	0.018758
SiO$_2$	Quartz	0.123985	0.499558	0.375574
Rh$_2$ZnO$_4$	Spinel	0.369029	0.330071	0.038958
Rh$_2$MgO$_4$	Spinel	0.360327	0.258765	0.101562
Rh$_2$CoO$_4$	Spinel	0.357971	0.333853	0.024119
Ni$_2$SiO$_4$	Spinel	0.234994	0.112817	0.122177
Al$_2$MgO$_4$	Spinel	0.249057	0.132738	0.116319
Rh$_2$CdO$_4$	Spinel	0.580161	0.756126	0.175965
MgTi$_2$O$_4$	Spinel	0.277899	0.620978	0.343079
CdV$_2$O$_4$	Spinel	0.582393	0.452657	0.129736
GeCo$_2$O$_4$	Spinel	0.266736	0.203161	0.063575
Cr$_2$CdO$_4$	Spinel	0.347283	0.362269	0.014986
CdIn$_2$O$_4$	Spinel	0.664341	0.375366	0.288975
AlNi$_2$O$_4$	Spinel	0.967221	0.984806	0.017585
ZnAl$_2$O$_4$	Spinel	0.220391	0.210962	0.00943
Mg$_2$VO$_4$	Spinel	0.348982	0.105376	0.243606
Ga$_2$ZnO$_4$	Spinel	0.307155	0.334726	0.027571
CaFeO$_3$	Tilted Perovskite	0.345664	0.30236	0.043304
BaNbO$_2$	Zircon	0.131521	0.430281	0.298761

The simple energy model allows for analytical derivatives, which we use to calculate the gradient and Hessian matrix of the potential energy surface at every point on a regular three dimensional grid. From each point on this grid we use gradient descent to identify a nearby stationary point, at which the magnitude of the gradient is zero. We then evaluate the eigenvalues of the Hessian matrix to identify whether the stationary point is a saddle point. From each saddle point gradient descent on the potential energy surface is used to identify the endpoints of a hop that passes through that saddle point. The set of possible hops is completed by applying symmetry operations to all known hops and linking sites that are close together (within 1 Angstrom) but are not already connected by a hop. We evaluate all pathways through the diffusion hop network that start at the site predicted to have the lowest energy and end at a translationally equivalent site. The path for which the maximum energy along the path is lowest is used to calculate the migration

energy, which is simply defined as the difference between the highest and lowest energy points along the path.

4. Band gaps and DFT+U calculations

In this section we show the calculated band gaps and the results of proton migration barriers using DFT+U and compared to the results without +U in the main text (Table 2). The DFT+U calculations were performed for $CrVO_4$-structured oxides that contain elements of Co, Cr, Fe, Mn, Ni, and V (Table 4-S). The U parameters were chosen according to Wang et al.[4] by fitting to experimental formation enthalpies. We have used the POTCAR files used by the Materials Project for the oxides containing Fe and Ni, because the DFT+U calculations had difficulty converging for these materials using the GW PAW POTCAR files we used in the rest of this work. The band gaps with and without DFT+U were calculated in the same way as other DFT calculations (see the Methodology section in the main text), followed by a static calculation by setting ICHARG=11 in VASP and using the charge density from the previously converged self-consistent run.

Table 4-S. Proton migration activation barrier and band gap for all 29 $CrVO_4$-structured oxides without and with DFT+U.

ICSD ID	Composition	DFT Activation Barrier without / with U (eV)	U value (eV)	Band gap without / with U (eV)
16618	$InPO_4$	0.340 / -	-	2.51 / -
16619	$TlPO_4$	0.270 / -	-	1.21 / -
16741[*]	$NiSO_4$	0.187 / 0.183	Ni: 6.2	3.97 / 4.93
16759	$MgSO_4$	0.234 / -	-	4.52 / -
18117	$MgCrO_4$	0.094 / 0.065	Cr: 3.7	2.15 / 2.49
18118	$CdCrO_4$	0.056 / 0.056	Cr: 3.7	2.03 / 2.31
23492	$CoCrO_4$	0.094 / 0.204	Co: 3.32, Cr: 3.7	0.03 / 1.51
23493[*]	$NiCrO_4$	0.053 / 0.061	Ni: 6.2, Cr: 3.7	0.71 / 1.92
23507[*]	$FeSO_4$	0.164 / 0.187	Fe: 5.3	2.12 / 4.07
25700[*]	$NiSeO_4$	0.188 / 0.209	Ni: 6.2	1.07 / 2.37
31231	$MnSO_4$	0.217 / 0.190	Mn: 3.9	2.60 / 3.86
33736	$CoSO_4$	0.229 / 0.235	Co: 3.32	3.40 / 4.53
36244	$CrVO_4$	0.172 / 0.100	V: 3.25, Cr: 3.7	0.52 / 1.79
60571	$CdSO_4$	0.177 / -	-	3.34 / -
62159	$CrPO_4$	0.242 / 0.326	Cr: 3.7	0.68 / 1.88
82282	$TiPO_4$	0.321 / -	-	0.01 / -
82286	VPO_4	0.196 / 0.188	V: 3.25	0.00 / 1.65
82161[*]	$FeVO_4$	0.129 / 0.102	V: 3.25, Fe: 5.3	0.03 / 3.11
89505	$LiMnO_4$	0.086 / 0.072	Mn: 3.9	1.32 / 1.53
109070	$MgSeO_4$	0.282 / -	-	2.87 / -
109071	$MnSeO_4$	0.165 / 0.226	Mn: 3.9	0.06 / 1.57
109072	$CoSeO_4$	0.256 / 0.195	Co: 3.32	0.57 / 2.00
109073	$CuSeO_4$	0.295 / -	-	1.35 / -
155065[*]	$FePO_4$	0.171 / 0.220	Fe: 5.3	0.03 / 5.07
155162	$InVO_4$	0.054 / 0.055	V: 3.25	3.02 / 3.12
159272	$AlPO_4$	0.161 / -	-	5.78 / -
166436	$TiSiO_4$	0.091 / -	-	1.54 / -
183216	$CuCrO_4$	0.154 / 0.089	Cr: 3.7	1.10 / 1.38
416147	$HgCrO_4$	0.085 / 0.073	Cr: 3.7	1.39 / 1.46

[*]These calculations were performed using the pseudopotential files used by the Materials Project.

5. VASP PAW potentials

Table 5-S provides a list of the VASP PAW potentials used in this work for each element.

Table 5-S. VASP PAW potentials used for each element.

Element	Pseudopotential
Ac	PAW_PBE Ac 06Sep2000
Ag	PAW Ag_GW 06Mar2008
Al	PAW Al_GW 19Mar2012
Am	PAW_PBE Am 08May2007
Ar	PAW Ar_GW 02Oct2006
As	PAW As_GW 20Mar2012
At	PAW At 21May2007
Au	PAW Au_GW 23Mar2010
B	PAW B 28Sep2005
Ba	PAW Ba_sv_GW 23Mar2010
Be	PAW Be_GW 04Mar2008
Bi	PAW Bi_GW 07Mar2011
Br	PAW_PBE Br 20Mar2012
C	PAW C_GW_new 19Mar2012
Ca	PAW Ca_sv_GW 31Mar2010
Cd	PAW Cd_f_GW 18May2010
Ce	PAW Ce_GW 26Mar2009
Cl	PAW Cl_GW 19Mar2012
Cm	PAW_PBE Cm 17Jan2011
Co	PAW Co_GW 31Mar2010
Cr	PAW_PBE Cr 06Sep2000
Cs	PAW Cs_sv_GW 23Mar2010
Cu	PAW Cu_GW 19May2006
Dy	PAW_PBE Dy 23Dec2003
Er	PAW_PBE Er 01Sep2006
Eu	PAW_PBE Eu 23Dec2003
F	PAW F_GW 19Mar2012
Fe	PAW Fe_GW 31Mar2010
Fr	PAW_PBE Fr_sv 29May2007
Ga	PAW Ga_GW 22Mar2012
Gd	PAW_PBE Gd 23Dec2003
Ge	PAW Ge 04Okt2005
H	PAW H_GW 21Apr2008
He	PAW He_GW 13May2007
Hf	PAW_PBE Hf 20Jan2003
Hg	PAW_PBE Hg_sv_GW 16Apr2014

Ho	PAW_PBE Ho 23Dec2003
I	PAW_PBE I_GW 12Mar2012
In	PAW_PBE In 08Apr2002
Ir	PAW_PBE Ir 06Sep2000
K	PAW K_sv_GW 31Mar2010
Kr	PAW Kr_GW 02Oct2006
La	PAW_PBE La 06Sep2000
Li	PAW Li_GW 11May2007
Lu	PAW_PBE Lu 23Dec2003
Mg	PAW Mg_GW 13Apr2007
Mn	PAW Mn_GW 31Mar2010
Mo	PAW_PBE Mo 08Apr2002
N	PAW N_GW_new 19Mar2012
Na	PAW_PBE Na 08Apr2002
Nb	PAW Nb_sv_GW 23Mar2010
Nd	PAW_PBE Nd 23Dec2003
Ne	PAW Ne_GW 02Oct2006
Ni	PAW Ni_GW 31Mar2010
Np	PAW_PBE Np 06Sep2000
O	PAW O_GW 19Mar2012
Os	PAW_PBE Os 17Jan2003
P	PAW P_GW 19Mar2012
Pa	PAW_PBE Pa 07Sep2000
Pb	PAW_PBE Pb 08Apr2002
Pd	PAW Pd_GW 06Mar2008
Pm	PAW_PBE Pm 23Dec2003
Po	PAW_PBE Po 10Feb2004
Pr	PAW_PBE Pr 23Dec2003
Pt	PAW Pt_GW 10Mar2009
Pu	PAW_PBE Pu 06Sep2000
Ra	PAW_PBE Ra_sv 29May2007
Rb	PAW Rb_sv_GW 23Mar2010
Re	PAW_PBE Re 17Jan2003
Rh	PAW Rh_GW 06Mar2008
Rn	PAW_PBE Rn 28Aug2006
Ru	PAW_PBE Ru 04Feb2005
S	PAW S_GW 19Mar2012
Sb	PAW Sb_GW 21Mar2012
Sc	PAW_PBE Sc 04Feb2005
Se	PAW Se_GW 20Mar2012
Si	PAW Si_GW 19Mar2012
Sm	PAW_PBE Sm 23Dec2003
Sn	PAW_PBE Sn 08Apr2002

Sr	PAW Sr_sv_GW 23Mar2010
Ta	PAW_PBE Ta 17Jan2003
Tb	PAW_PBE Tb 23Dec2003
Tc	PAW_PBE Tc 04Feb2005
Te	PAW Te_GW 22Mar2012
Th	PAW_PBE Th 07Sep2000
Ti	PAW_PBE Ti 08Apr2002
Tl	PAW_PBE Tl 08Apr2002
Tm	PAW_PBE Tm 23Dec2003
U	PAW_PBE U 06Sep2000
V	PAW_PBE V 08Apr2002
W	PAW_PBE W 08Apr2002
Xe	PAW Xe_GW 08Jan2009
Y	PAW Y_sv_GW 23Mar2010
Yb	PAW_PBE Yb 23Dec2003
Zn	PAW Zn_GW 09Oct2010
Zr	PAW Zr_sv_GW 07Apr2010

6. References

1.   Butterworth-Heinemann, Oxford, 1997.
2.   C. Colinet, K. Inden and R. Kikuchi, *Acta metall. mater.*, 1993, **41**, 1109-1118.
3.   M. O'Keefe and N. E. Brese, *Journal of the American Chemical Society*, 1991, **113**, 3226-3229.
4.   L. Wang, T. Maxisch and G. Ceder, *Physical Review B*, 2006, **73**, 195107.